

Fractional-order heterogeneous memristive Rulkov neuronal network and its medical image watermarking application

Dawei Ding(丁大为), Yan Niu(牛炎), Hongwei Zhang(张红伟), Zongli Yang(杨宗立), Jin Wang(王金), Wei Wang(王威), and Mouyuan Wang(王谋媛)

Citation: Chin. Phys. B, 2024, 33 (**5**): 050503. DOI: 10.1088/1674-1056/ad322b
Journal homepage: http://cpb.iphy.ac.cn; http://iopscience.iop.org/cpb

What follows is a list of articles you may be interested in

Analysis of anomalous transport with temporal fractional transport equations in a bounded domain

Kaibang Wu(吴凯邦), Jiayan Liu(刘嘉言), Shijie Liu(刘仕洁), Feng Wang(王丰), Lai Wei(魏来), Qibin Luan(栾其斌), and Zheng-Xiong Wang(王正汹)

Chin. Phys. B, 2023, 32 (**11**): 110502. DOI: 10.1088/1674-1056/acedf3

A novel fractional-order hyperchaotic complex system and its synchronization

Mengxin Jin(金孟鑫), Kehui Sun(孙克辉), and Shaobo He(贺少波)

Chin. Phys. B, 2023, 32 (**6**): 060501. DOI: 10.1088/1674-1056/acc0f6

Finite-time complex projective synchronization of fractional-order complex-valued uncertain multi-link network and its image encryption application

Yong-Bing Hu(胡永兵), Xiao-Min Yang(杨晓敏), Da-Wei Ding(丁大为), and Zong-Li Yang(杨宗立)

Chin. Phys. B, 2022, 31 (**11**): 110501. DOI: 10.1088/1674-1056/ac7869

The dynamics of a memristor-based Rulkov neuron with fractional-order difference

Yan-Mei Lu(卢艳梅), Chun-Hua Wang(王春华), Quan-Li Deng(邓全利), and Cong Xu(徐聪)

Chin. Phys. B, 2022, 31 (**6**): 060502. DOI: 10.1088/1674-1056/ac539a

Analysis and implementation of new fractional-order multi-scroll hidden attractors

Li Cui(崔力), Wen-Hui Luo(雒文辉), and Qing-Li Ou(欧青立)

Chin. Phys. B, 2021, 30 (**2**): 020501. DOI: 10.1088/1674-1056/abbbe4

Fractional-order heterogeneous memristive Rulkov neuronal network and its medical image watermarking application

Dawei Ding(丁大为), Yan Niu(牛炎), Hongwei Zhang(张红伟)†, Zongli Yang(杨宗立), Jin Wang(王金), Wei Wang(王威), and Mouyuan Wang(王谋媛)

School of Electronics and Information Engineering, Anhui University, Hefei 230601, *China*

(Received 26 December 2023; revised manuscript received 22 February 2024; accepted manuscript online 11 March 2024)

This article proposes a novel fractional heterogeneous neural network by coupling a Rulkov neuron with a Hopfield neural network (FRHNN), utilizing memristors for emulating neural synapses. The study firstly demonstrates the coexistence of multiple firing patterns through phase diagrams, Lyapunov exponents (LEs), and bifurcation diagrams. Secondly, the parameter related firing behaviors are described through two-parameter bifurcation diagrams. Subsequently, local attraction basins reveal multi-stability phenomena related to initial values. Moreover, the proposed model is implemented on a microcomputer-based ARM platform, and the experimental results correspond to the numerical simulations. Finally, the article explores the application of digital watermarking for medical images, illustrating its features of excellent imperceptibility, extensive key space, and robustness against attacks including noise and cropping.

Keywords: fractional order, memristors, Rulkov neuron, medical image watermarking

PACS: 05.45.–a, 87.18.Sn, 05.45.Vx **DOI:** 10.1088/1674-1056/ad322b

1. Introduction

The human brain is a complex dynamic system containing billions of interconnected neurons that exhibit intricate and chaotic dynamics.[1] Research reveals a strong correlation between these chaotic dynamics and neurological disorders such as epilepsy. For instance, healthy people usually show chaotic patterns in their brain activity (measured by electroencephalogram), whereas people with epilepsy often show more regular, periodic patterns.[2,3] Studying the chaotic dynamics of the nervous system, a vital step to comprehend the origin of neuronal diseases, holds significant theoretical and practical implications.[4] To study and emulate the critical dynamic characteristics of neurons, several mathematical models have been established by researchers, which encompass the Hindmarsh–Rose (HR) model,[5] FitzHugh–Nagumo (FHN) model,[6] Rulkov model,[7,8] and the Izhikevich model.[9] The development and application of these models significantly advance the field of neurophysiology, which contribute to a deeper understanding of the complex dynamics of the human brain.

Memristors can emulate neural synapses or magnetic induction, especially when cell activities involve the movement of extracellular and intracellular ions.[10] Neurons can communicate not only through electrical and chemical connections but also directly through gap junctions. These junctions, acting as bridges, allow ions to pass between neurons and can be influenced by electromagnetic fields. The Hodgkin–Huxley (HH) model[11,12] and Morris–Lecar model[13,14] are constructed based on the ion channels of neurons, and their stochastic ion channels can be simulated using memristors.[15,16] In order to incorporate the effects of electromagnetic induction, modifications have been made to these neuronal models, establishing a connection between magnetic flux and membrane potential using memristors.[17] Such modifications have been applied to FitzHugh–Nagumo (FHN),[18] Hodgkin–Huxley (HH),[19,20] and HR[21–23] neurons. Most neuron models capture essential dynamic properties and firing patterns observed in biological cells, but have limited exploration of physical field effects. Incorporating memristors into neural circuits is seen as a promising approach for estimating biophysical effects. Kumar *et al.* provided empirical evidence showing the substantial improvement in convergence efficiency and solution accuracy of Hopfield neural network (HNN) through the integration of memristors.[24] Hong *et al.* introduced a novel method using memristors to simulate neurotransmitter modulation, facilitating the creation of a self-repairing astrocyte-neuron network.[25] Furthermore, integrating memristors into cellular neural networks significantly enhances performance, notably speeding up pattern recognition and image processing tasks.[26] In summary, memristors have attracted a great deal of interest in research and have become crucial components in neuromorphic circuits.

The concepts of multi-stability is complex and fascinating elements in the study of dynamic systems.[27,28] The analysis suggests that this kind of behavior, which can exhibit either identical or diverse topological properties, is further characterized by the presence of numerous attractors located at different positions.[29,30] Recently, researchers like Lin *et al.* have integrated two distinct characteristics of memristors as

†Corresponding author. E-mail: hwzhang@ahu.edu.cn

© 2024 Chinese Physical Society and IOP Publishing Ltd

external stimuli into the HNN, allowing for control over the number of attractors in hyperchaotic systems.[31] Moreover, the constructed high-dimensional system finds its application in brain-like image encryption, thereby demonstrating the impressive complexity inherent in the memristor neural network system. Introducing a non-ideal magnetron memristor model into the HNN leads to the simultaneous presence of diverse attractors and amplitude control phenomena, encompassing multi-stability.[32]

The organization of this article is as follows: In Section 2, a fractional-order memristor model is developed and subsequently utilized to construct an FRHNN model. In Section 3, an analysis is conducted on region transitions, taking into consideration factors such as magnetic induction, memristor initial state, and system order. In Section 4, a validation of the systems is carried out using a digital implementation approach on the ARM platform. Section 5 describes an enhanced medical image watermark application, utilizing chaotic sequences and a hybrid scheme. Finally, Section 6 concludes the article.

2. Fractional-order memristive neuron model

In this section, we introduce a fractional-order memristor for neuronal synapse simulation and transform the discrete Rulkov model into a continuous form. This continuous Rulkov neuron is then coupled with an HNN through the memristor, forming a new heterogeneous neural network.

2.1. Fractional-order memristor

A fractional continuous flux-controlled memristor model is proposed to simulate electromagnetic induction in Ref. [22]. The model is expressed as

$$\begin{cases} i = \left(\alpha + \beta\varphi^2\right) v, \\ D^q\varphi = \varphi + \varepsilon v, \end{cases} \tag{1}$$

where i, v respectively, represent the current flowing through the memristor and the voltage across it. φ represents the internal state variable of the memristor. The parameters of memristor are denoted as α and β. The parameter ε represents the time scale factor of the induced electromotive force in a finite transient period, and it depends on the property of the medium.

2.2. Fractional-order system

The Rulkov neural model, which was initially structured as a two-dimensional discrete mapping, has evolved into a continuous system through progressive dynamic changes.[33] This research has established that the continuous nonlinear model exhibits greater sensitivity to its dynamic characteristics. The aforementioned publication introduces the continuous Rulkov network model, which is presented as follows:

$$\begin{cases} D^q x_1 = \dfrac{\alpha}{1+x_1^2} - x_1 + y_1, \\ D^q y_1 = -\sigma x_1 - \beta, \end{cases} \tag{2}$$

where x_1 represents the membrane potential, while y_1 represents the gating process. The system is characterized by three parameters: α, β, and σ. Notably, β is referred to as the applied stimulus.

The Hopfield neural network can be represented by the circuit state equation for n neurons. Specifically, the state equation of the circuit for the i-th neuron can be mathematically expressed as

$$C_i \frac{\mathrm{d}x_i(t)}{\mathrm{d}t} = -\frac{x_i(t)}{R} + \sum_{j=1}^{n} w_{ij} \tanh\left(x_j(t)\right) + I_i, \tag{3}$$

where x_i represents the state variable for the voltage across capacitor C_i. R_i represents the resistance between the inside and outside of the neuron, and I_i denotes the input bias current. The input signal of the j-th neuron processed by the neuronal activation function is represented by $\tanh\left(x_j(t)\right)$. The synaptic weight matrix, denoted as $W = w_{ij}$ represents the strength of the connection between the i-th and j-th neurons, with dimensions $n \times n$. The model can be expressed as follows:

$$\begin{cases} D^q x_2 = p_1 \cdot \tanh\left(x_2\right) + p_2 \cdot \tanh\left(y_2\right) + p_3 \cdot \tanh\left(z_2\right), \\ D^q y_2 = p_4 \cdot \tanh\left(x_2\right) + p_5 \cdot \tanh\left(y_2\right) + p_6 \cdot \tanh\left(z_2\right), \\ D^q z_2 = p_7 \cdot \tanh\left(x_2\right) + p_8 \cdot \tanh\left(y_2\right) + p_9 \cdot \tanh\left(z_2\right), \end{cases} \tag{4}$$

where p_1, p_2, p_3, p_4, p_5, p_6, p_7, p_8, p_9 are the parameters of the system.

The analysis in this article on the interconnected dynamic behaviors of various neurons is important. Neural synapses play a crucial role in signal transmission and information encoding within neurons and neural networks. To emulate this process, the researchers utilized a magnetic flux-controlled memristor, that displays synapse-like traits, acting as the potential difference between the membranes of two neurons. As illustrated in Fig. 1, neuron 1 and neuron 2 represent two neurons in different regions of the brain, which are connected through synapses within their respective neural networks. The mathematical model of the biconnected neuronal system with memristor is presented below:

$$\begin{cases} D^q x_1 = \dfrac{\alpha}{1+x_1^2} - x_1 + y_1 - k\tanh\left(\varphi\right)\left(x_1 - x_2\right), \\ D^q y_1 = -\sigma x_1 - \beta, \\ D^q \varphi = \mu\left(x_1 - x_2\right), \\ D^q x_2 = -x_2 + p_1 \cdot \tanh\left(x_2\right) + p_2 \cdot \tanh\left(y_2\right) \\ \qquad + p_3 \cdot \tanh\left(z_2\right) + k\tanh\left(\varphi\right)\left(x_1 - x_2\right), \\ D^q y_2 = -y_2 + p_4 \cdot \tanh\left(x_2\right) \\ \qquad + p_5 \cdot \tanh\left(y_2\right) + p_6 \cdot \tanh\left(z_2\right), \\ D^q z_2 = -z_2 + p_7 \cdot \tanh\left(x_2\right) \\ \qquad + p_8 \cdot \tanh\left(y_2\right) + p_9 \cdot \tanh\left(z_2\right), \end{cases} \tag{5}$$

where the nonlinear term $k\tanh\left(\varphi\right)\left(x_1 - x_2\right)$ represents the induced currents between two adjacent neurons. x_1 and x_2 pos-

sess different membrane potentials. Here, k represents the coupling strength associated with the memristor's magnetic induction effect.

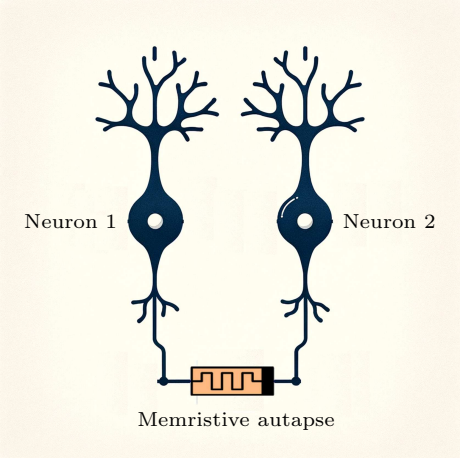


Fig. 1. Memristor-based synaptic connection.

3. Firing patterns of FRHNN system under different parameters

In this section, the Adomian decomposition method (ADM) is applied for simulating and examining system (5) including the two-parameter bifurcation diagrams, spectral entropy (SE) complexity, bifurcation diagrams, LEs, phase diagrams, time series plots, *etc*. The objective is to analyze the firing behaviors of a fractional heterogeneous memristive Rulkov neuronal network under varying parameters and initial values. The simulation employs a fixed time-step of 0.01 seconds and spans a time range from 4000 seconds to 5000 seconds. To calculate the finite-time Lyapunov exponent, we use Wolf's Jacobian-based method with a fixed time-step of 0.01 seconds, continuing the simulation until reaching 4000 seconds.

3.1. Dynamics related to system order

Fractional-order systems display more complex dynamics than integer-order systems. In this context, the order q is a crucial factor for examining the firing patterns in fractional-order chaotic systems. We use q as a bifurcation parameter to explore the different bifurcation behaviors that occur under various initial conditions. This approach helps to understand the system's behavior in a more detailed manner.

In system (5), set $\alpha = 13$, $\beta = 0$, $\sigma = 3$, $\mu = 1$, $p_1 = 3$, $p_2 = -3.8$, $p_3 = 3.5$, $p_4 = 3.5$, $p_5 = 1.7$, $p_6 = 3.2$, $p_7 = 1$, $p_8 = -2$, $p_9 = -8.3$, and $k = 0.5$. It should be noted that red, green, and blue in Figs. 2(a) and 2(b) represent the initial values $(0,0,-12,0,0,0)$, $(0,0,-2.14,0,0,0)$, and $(0,0,18.5,0,0,0)$, individually.

Figure 2(a) exhibits different firing patterns under different initial conditions. It can be seen that when $q \in [0.62, 0.7]$, they respectively exhibit period-1, period-2, and chaotic firing patterns. Figure 2(b) shows the maximum Lyapunov exponent (MLE) diagram corresponding to the firing patterns depicted in Fig. 2(a). In Fig. 2(c), we can observe that under the initial condition $(0,0,18.5,0,0,0)$, the system starts from a chaotic firing pattern and gradually transitions to a period-2 pattern after $q = 0.73$, then undergoes a sudden change to a period-3 pattern at $q = 0.87$.

Figure 3 displays the projections of coexisting multiple firing patterns of system (5) at specific parameter values q on the x_1–y_1 plane. In this figure, the red, green, and blue orbits correspond to initial values $(0,0,-12,0,0,0)$, $(0,0,-2.14,0,0,0)$, and $(0,0,18.5,0,0,0)$, respectively. Subsequently, it becomes evident that figure 3 illustrates the coexistence of quasi-period, different period firings, and chaotic firing patterns.

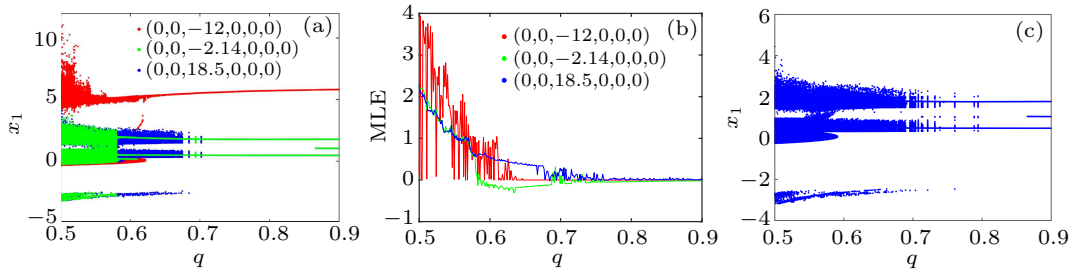


Fig. 2. Coexisting multiple bifurcation behaviors for $q \in [0.5, 0.9]$. (a) The bifurcation diagram under different initial values, (b) the LEs diagram under different initial values, (c) the bifurcation diagram under initial value $(0,0,18.5,0,0,0)$.

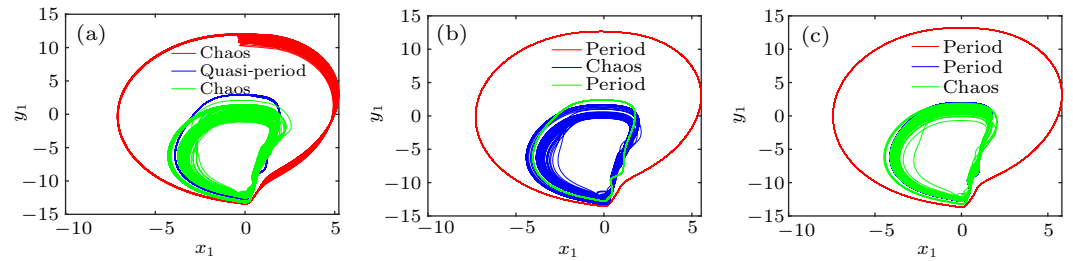


Fig. 3. Coexisting attractors of x_1–y_1 plane under different initial values, the red corresponds to the initial value $(0,0,-12,0,0,0)$, the green to $(0,0,-2.14,0,0,0)$, and the blue to $(0,0,18.5,0,0,0)$. (a) $q = 0.6$, (b) $q = 0.7$, (c) $q = 0.9$.

3.2. Dynamics related to memristor synapse

When the order q are set to 0.9, the coupling strength parameter k is specified as bifurcation parameter. The initial values is set as $(0,0,0,0,0,0)$. The other parameters of system (5) are consistent with Subsection 3.1. When changing the coupling strength parameter k in the region $[-1,1.5]$, the bifurcation diagrams of k are numerically depicted in Fig. 4(a). The MLE is drawn in Fig. 4(b).

In Fig. 4(a), the system starts from a period-2 pattern and transitions into a chaotic firing pattern at $k=-0.78$. Within the range of k from -0.78 to -0.53, the system exhibits chaotic firing patterns, oscillating repeatedly around points near multiple trajectories. Following that, in the interval where k ranges from -0.53 to -0.36, the system enters a period-5 pattern. After a brief chaotic region, from -0.36 to -0.27, it returns to the period-2 pattern. When the coupling strength k reaches 0, the system enters a silence pattern, displaying stable points. As k is further increased, the system undergoes a chaotic crisis at $k=0.21$, leading to chaotic firing patterns. Subsequently, the system exhibits a period-3 firing pattern at $k=0.48$. After experiencing a brief chaotic window, it transitions to a period-5 firing pattern at $k=1.16$. With further increases in $k=1.31$, through period-doubling bifurcation routes, the system experiences another chaotic crisis at $k=1.4$, transitioning into the next chaotic firing pattern. The finite-time MLE displayed in Fig. 4(b) corresponds closely to the bifurcation diagram. Figure 5 shows their phase portraits on the x_1–y_1 plane and the corresponding time series of the membrane potential x_1 with several specific discrete values of k. Figures 5(a)–5(d) are diagrams at periodic spiking firing pattern, chaotic bursting firing pattern, periodic bursting firing pattern, and chaotic spiking firing pattern individually indicating that the FRHNN system has rich electrical activities.

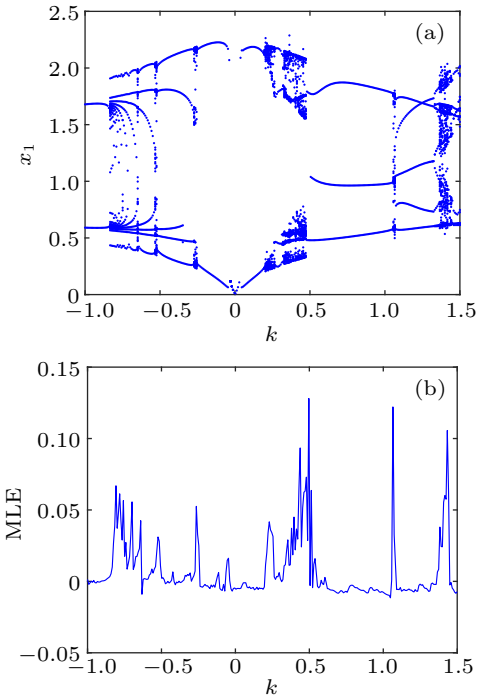


Fig. 4. The dynamics for $k\in[-1,1.5]$. (a) The bifurcation diagram, (b) the MLE diagram.

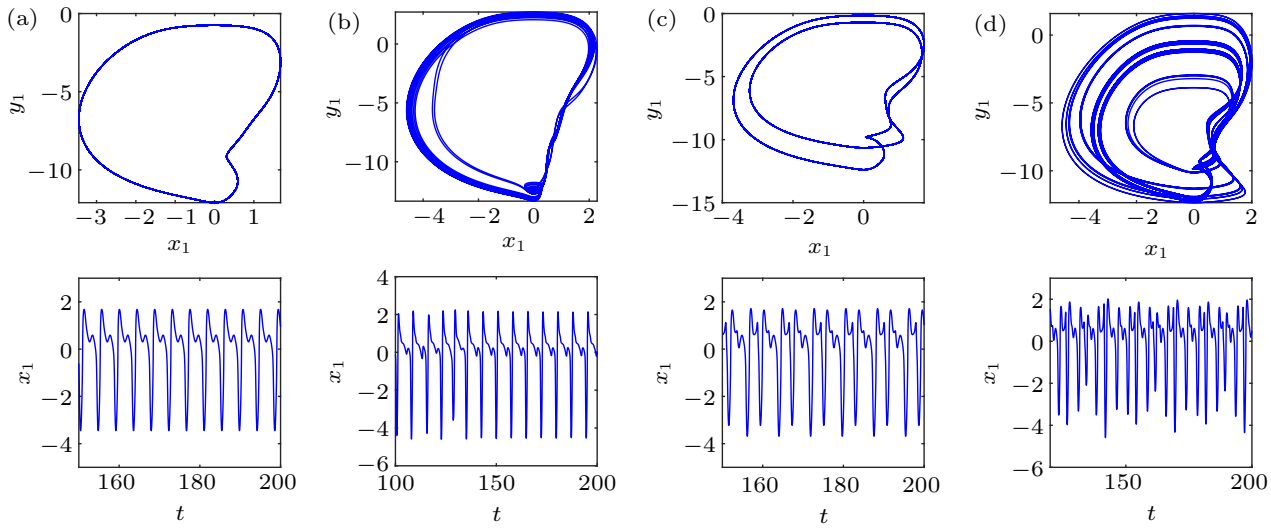


Fig. 5. Phase diagrams on the x_1–y_1 plane and membrane potential time series for neuronal firing patterns with different values of k. (a) $k=-1$, (b) $k=0.2$, (c) $k=1.2$, (d) $k=1.4$.

In addition, the phenomena of transient chaotic attractors are found in the FRHNN system. The time domain spectra and attractors of the proposed system are shown in Fig. 6. Set $k=0.48$. It can be seen from Fig. 6(a) that the attractor first oscillates in chaos and eventually stabilizes at period-2 pattern. When we set $k=-0.05$, as can be seen from Fig. 6(b), with the change of time t, the attractors first enters the chaotic pattern, then passes through the transition state and quasi-period, and eventually stabilizes at period-2 pattern. In Fig. 6, the transient chaotic attractor eventually stabilizes at different periodic patterns, indicating that the proposed system has rich dynamic phenomena.

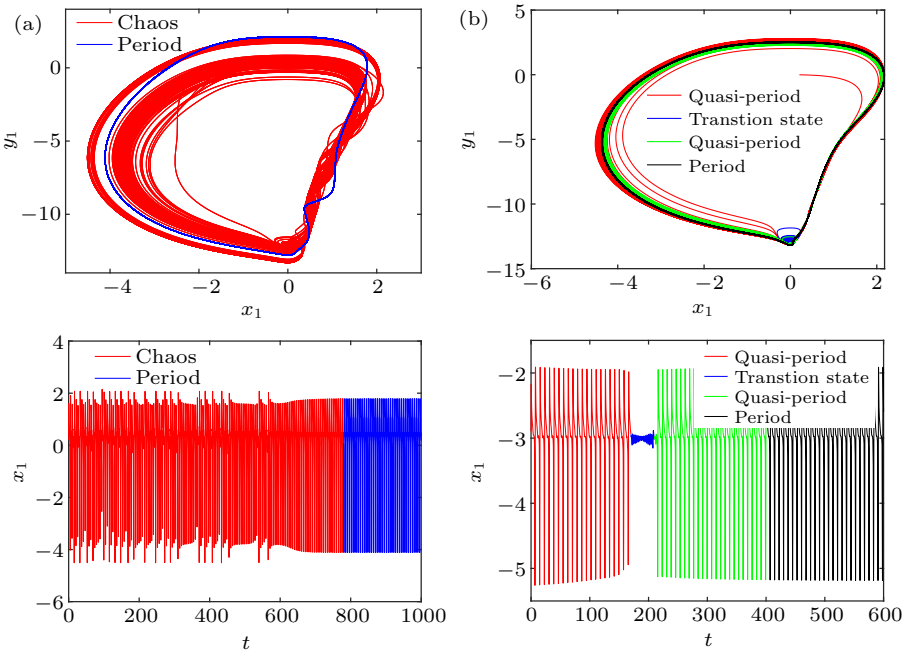


Fig. 6. Phase diagram and time domain spectrum of transient chaotic attractor: (a) $k = 0.48$, (b) $k = -0.05$.

3.3. Firing patterns depends on the initial-related parameters

Subsections 3.1 and 3.2 demonstrate that changes in parameters affect the firing behavior of system (5). This section delves into how alterations in parameters q and k impact the nervous system's dynamics, utilizing two-parameter bifurcation diagrams for analysis.

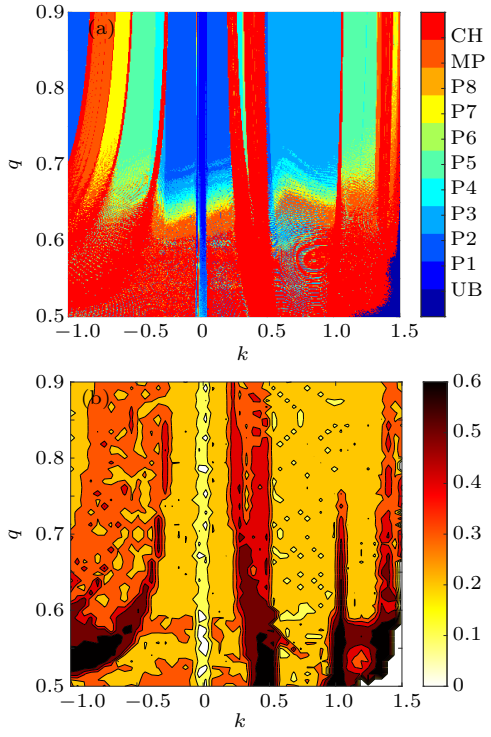


Fig. 7. The dynamics on k–q plane. (a) Two-parameters bifurcation diagram, (b) SE complexity diagram.

When the initial values are set to $(0,0,0,0,0,0)$ in system (5), a two-parameter bifurcation diagram on k–q plane is created through numerical simulation. The other parameters are consistent with those in Subsection 3.1. In Fig. 7(a), the UB stands for unbounded behavior; the P1 to P8 stand for period-1 to period-8; the MP stands for multiple periods with a cycle number of more than 8; the CH denotes chaos. In Fig. 7(b), the SE complexity map shows that darker colors represent higher complexity, with the high-complexity regions corresponding to chaotic patterns, while the low-complexity areas correspond to periodic patterns. Figure 7(b) confirms the firing patterns in the two-parameter bifurcation plot of Fig. 7(a). Figure 7(a) effectively illustrates the dynamic behavior of the system under different conditions of k and q, showcasing how changes in these parameters influence the system's state transitions.

3.4. Local attraction basins

By measuring the firing pattern, the attraction basin of the initial condition domain can be obtained, in which different types of dynamic states are marked with different colors. The other parameters of system (5) are consistent with Subsection 3.2. For the coupling strength $k = 0.5$ in the FRHNN system, the local attraction basin in the $x_1(0)$–$y_1(0)$ plane with $(x_2(0), \varphi(0), y_2(0), z(0)) = (0,0,0,0)$ is shown in Fig. 8, where different color regions represent different attractors. In Fig. 8(a), the attraction basin in the plane areas of $x_1 \in (-20,20)$ and $y_1 \in (-20,20)$ is drawn, in which the orange area represents chaos, the light blue area represents period-3, the blue area represent period-2 and the other area are consistent with Fig. 7(a). In Fig. 8, the widely distributed points of other different colors represent other distinct firing patterns. According to the above analysis, different attractors

coexist in the proposed system, so the proposed system has multistable behaviors.

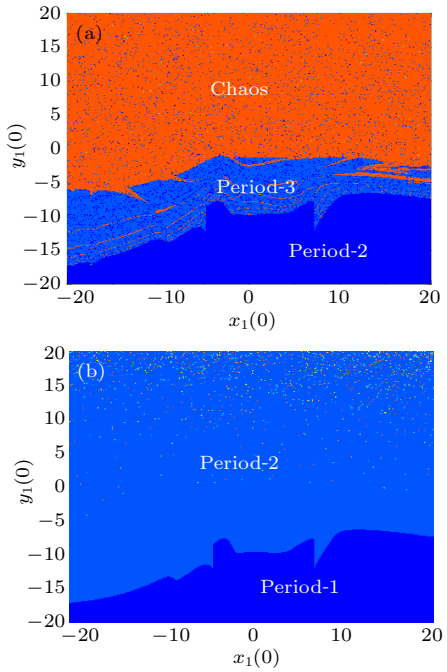


Fig. 8. The local attraction basins in $x_1(0)$–$\varphi(0)$ initial plane: (a) $q = 0.65$, (b) $q = 0.9$.

4. ARM implementation of fractional-order heterogeneous memristive Rulkov neuronal models

Digital electronic technology is a highly effective approach for supporting the intricate dynamical characteristics exhibited by complex nonlinear systems. In this section, we perform a hardware circuit experiment on the memristive neuron system. As depicted in Fig. 9(b), the hardware circuit primarily comprises the TLV5618 digital-to-analog converter and the STM32F750 microcomputer. The STM32F750 single-chip microcomputer facilitates digital computations, while the digital-to-analog converter transmits two output signals. The main control chip employed is the 32-bit ARM Cortex-M7 microcomputer, capable of reaching a maximum core frequency of 216 MHz. Its single-cycle multiplication instruction enables the complete realization of the iterative equation for the memristive neuron model.

The flow diagram illustrating the implementation of the fractional-order system is depicted in Fig. 9(a), accompanied by system (5) that provides a necessary iterative algorithm for the FRHNN model. The discrete iterative equation is realized using the C language and then the program is downloaded to the ARM development board. During the step of data processing, all data is converted to analog signals. To minimize the impact of data processing on the iterative computation, the operations of pushing and popping are introduced. This involves storing and protecting the values of state variables at a memory location indicated by a stack pointer. In real-world applications, suitable values for the parameters q and k can be chosen based on the aforementioned complexity results or bifurcation analysis. Additionally, for the implementation on the STM32F750 ARM development board, specific considerations and optimizations may need to be taken into account.

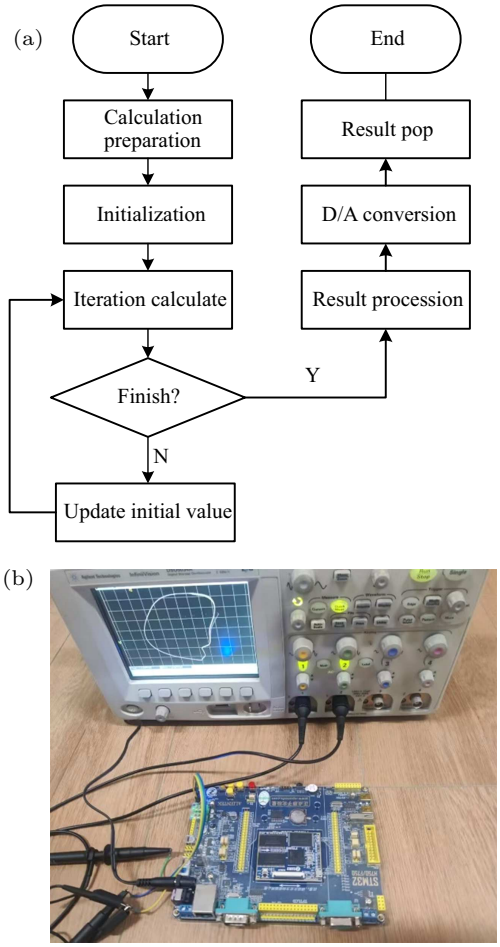


Fig. 9. The digital implementation: (a) program flow for ARM implementation, (b) digital circuit experimental platform.

With fixed control parameters, the control chip generates output signals that are controlled by two digital-to-analog converter (DAC) modules. Initially, we define two arrays for variable calculation. Subsequently, to achieve iterative calculation, the elements of the array are updated based on other discrete equations, following the initialization of the first element. Finally, the variable is written into the control register of the DAC to directly obtain the corresponding analog voltage. The resulting analog signals are then captured and displayed on an oscilloscope, revealing the typical attractor phase trajectories under different system states. Specifically, figure 9(b) illustrates the periotic attractors generated, while figure 10 shows the case of the chaotic attractor, periotic attractor, and chaotic attractor generated. The coexistence of diverse states, as demonstrated in Fig. 3, is successfully realized in Fig. 10. The circuit implementation results align closely with the simulation results, affirming the feasibility of physically realizing this model.

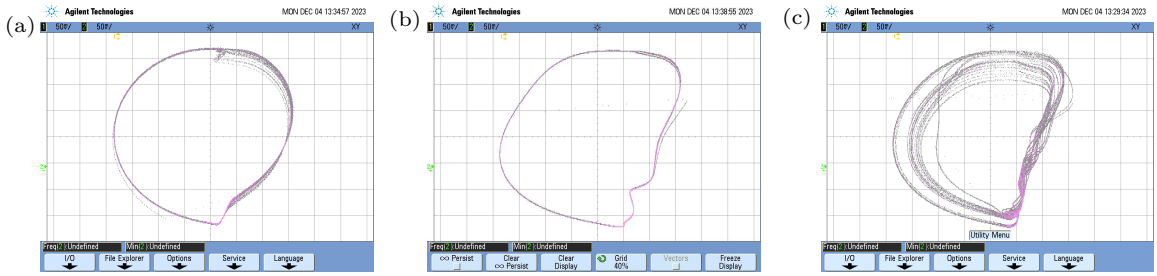


Fig. 10. ARM implementation of the coexisting firing patterns with different initial value: (a) $(0,0,-12,0,0,0)$, (b) $(0,0,-2.14,0,0,0)$, (c) $(0,0,18.5,0,0,0)$.

5. Medical image watermarking application

This section proposes an image encryption scheme, which consists of four parts: secret key and chaotic sequence generation, embedding, extraction and encryption/ decryption processes. The overall process is presented in Fig. 11.

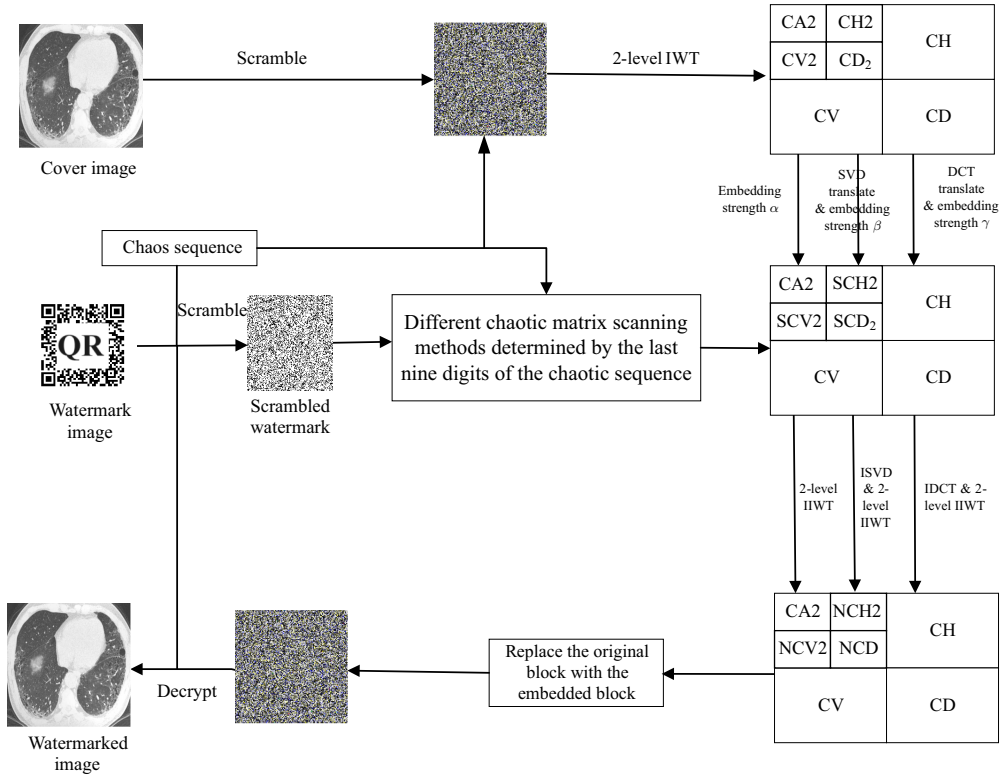


Fig. 11. Watermark embedding algorithm flowchart.

5.1. Medical image encryption scheme

The proposed digital watermarking scheme combines chaotic sequences, discrete cosine transform (DCT), integer wavelet transform (IWT), and singular value decomposition (SVD) to enhance the security and robustness of watermarking medical images. By integrating a chaotic sequence, a secure watermark extraction process is ensured. Additionally, the combined utilization of DCT, IWT, and SVD offers resistance against common image processing techniques applied to medical images, such as JPEG compression and various transformations. Moreover, the incorporation of quick response codes (QR codes) provides advantages such as high data capacity, error correction capabilities, and fast readability.

Step 1 Read a medical image with size $M \times N$ and save as a matrix $\boldsymbol{P}$ in 2D size $M \times N$.

Step 2 Select controlling parameters in the range of generating chaos and choose specific parameters induction strength α, memristor initial state β, and fractional order γ as the security key. The key values are set as $(\alpha,\beta,\gamma) = (1.2,0.5,0.8)$. Then, one can obtain the chaotic sequences S.

Step 3 Transform the chaotic sequences S to the pseudo-random sequences S_1 within the range of $[0,255]$, respectively. The transform relations are given as follows:

$$S_1 = \text{floor}\left((S+50)\times 10^{16}\right) \mod 256. \tag{6}$$

Step 4 The watermark image and medical image are reorganized based on the sorting determined by matrices I and J, following the steps outlined in Algorithm 1.

Algorithm 1 Shuffle the pixels.

Input: A pre-processed image $\boldsymbol{P}$ of size $M \times N$, a random chaotic sequence matrix $\boldsymbol{S}$.

1: Sort each row of $\boldsymbol{S}$ to obtain I;
2: Sort each column of $\boldsymbol{S}$ to obtain J;
3: for $i = 1$ to M do
4: for $j = 1$ to N do
5: row $= \mathrm{mod}\left(I_{i,j} + 2 \times J_{i,j}, M\right) + 1$
6: col $= \mathrm{mod}\left(j_{i,j} + I_{i,j}, N\right) + 1$
7: $B_{i,j} = P_{\mathrm{row,col}}$
8: end
9: end

Output: The pixels shuffled result T.

Step 5 Starting our digital watermark embedding process, we initiate with a two-level IWT transformation on the input image, producing subbands CA, CH, CV, and CD.

Step 6 In the CH subband, CH2 is subjected to a DCT transformation, and the CV2 subband undergoes an SVD transformation, before embedding. Additionally, direct embedding is applied to the CD2 subband.

Step 7 Subsequently, the embedded layers undergo an IDCT transformation for the CH2 subband and an ISVD transformation for the CD2 subband. Following these transformations, two successive IIWT processes are applied. The resulting layers, post-embedding, replace their respective original layers.

Step 8 By decrypting, the image with the embedded watermark can be retrieved.

Step 9 Extraction is the inverse process of embedding.

5.2. Security analysis

Figure 12 demonstrates the effects of utilizing chaos index scrambling alone. The chaos index scrambling effectively disrupts the correlation between pixels, which are significant advantages of this approach.

The similarity between the original host image and the watermarked image can also be assessed using histograms. The embedded watermark is imperceptible, ensuring the integrity of the host information remains unaffected. As illustrated in Fig. 13, the histograms of the host image and its watermarked counterpart exhibit high similarity. Meanwhile, the peak signal-to-noise ratio (PSNR) is a metric used to evaluate the similarity between the cover image and the watermarked one, assessing the imperceptibility of the watermark. As a general rule, when PSNR exceeds 40 dB, it guarantees that the watermark is imperceptible.[34] In this study, the PSNR between the original and watermarked images is 45.5636 dB, substantiating the watermark's imperceptibility. This demonstrates that the new embedding rule employed in the watermarking scheme offers excellent imperceptibility.

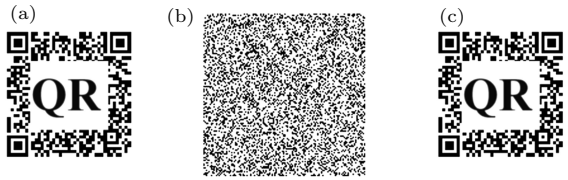


Fig. 12. Security test of the scrambled watermark: (a) original watermark, (b) scrambled watermark with chaos sequence, (c) extracted watermark.

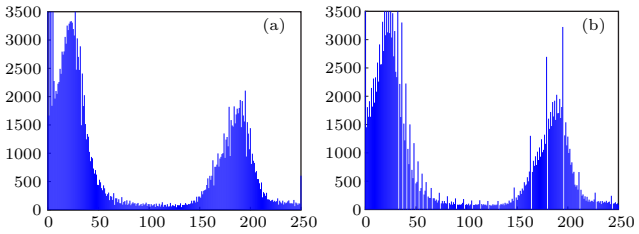


Fig. 13. Histograms: (a) cover image, (b) watermarked image.

5.3. Attack testing analysis

To assess the resilience of the proposed watermarking method, several typical image attacks are applied to the watermarked image. Figure 14 shows cropping, salt-and-pepper noise, and brightness/contrast attacks. Despite the degradation in the quality of the extracted watermark as increasing attack intensity on the watermarked images, the proposed scheme demonstrates resilience against attacks. The extracted watermark remains visually recognizable to human observers.

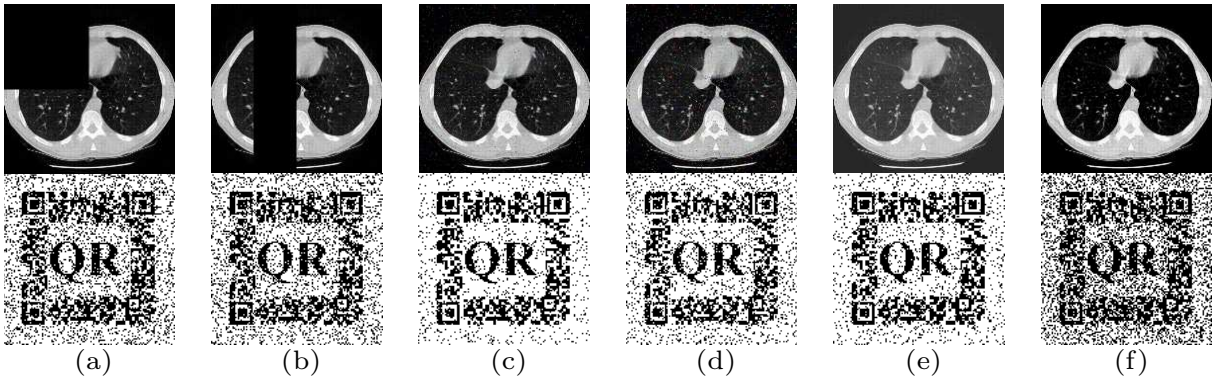


Fig. 14. Images under different attacks and extracted watermark images: (a) cropping attack on the left upper quarter, (b) vertical cropping attack on 1/4 of the image, (c) salt-and-pepper noise attack with intensity 0.01, (d) salt-and-pepper noise attack with intensity 0.02, (e) brightness attack with intensity 0.15, (f) contrast attack with intensity 0.1.

6. Conclusion

In this article, we presented a new heterogeneous FRHNN model by using memristors to simulate neural synapses. Initially, the study shows the coexistence of multiple firing patterns through phase diagrams, LEs, and bifurcation diagrams. It then describes firing behaviors related to parameter and initial condition with two-parameter bifurcation diagrams and local basin diagrams. The model is implemented on an ARM platform, with experimental results closely matching numerical simulations. Furthermore, this study introduces an innovative medical image watermarking scheme that leverages chaotic sequences based on the proposed neural network model, offering enhanced security performance. Considering the needs of practical applications, our focus will shift more towards the implementation of deep learning.

Data availability statement

The authors confirm that the data supporting the findings of this study are available within the article.

References

[1] Preissl H, Lutzenberger W and Pulvermüller F 1996 *Brain Sci.* **19** 307
[2] Lehnertz K and Elger C E 1998 *Phys. Rev. Lett.* **80** 5019
[3] Mormann F, Andrzejak R G, Elger C E and Lehnertz K 2007 *Brain* **130** 314
[4] Breakspear M 2006 *Aust. N. Z. J. Psychiatry* **40** 20
[5] Li Z J, Xie W Q, Zeng J F and Zeng Y C 2023 *Chin. Phys. B* **32** 010503
[6] Xu Q, Chen X J, Chen B, Wu H G, Li Z and Bao H 2023 *Nonlinear Dyn.* **111** 8737
[7] Lu Y M, Wang C H, Deng Q L and Xu C 2022 *Chin. Phys. B* **31** 060502
[8] Rulkov N F 2002 *Phys. Rev. E* **65** 041922
[9] Muni S S, Rajagopal K, Karthikeyan A and Arun S 2022 *Chaos, Solitons & Fractals* **155** 111759
[10] Bao H, Hu A H, Liu W B and Bao B C 2020 *IEEE Trans. Neural Netw. Learning Syst.* **31** 502
[11] Deng H Y, Gui R and Yao Y G 2023 *Chin. Phys. B* **32** 120501
[12] Hodgkin A L and Huxley A F 1952 *The Journal of Physiology* **117** 500
[13] Behdad R, Binczak S, Dmitrichev A S, Nekorkin V I and Bilbault J M 2015 *IEEE Trans. Neural Netw. Learning Syst.* **26** 1875
[14] Morris C, Lecar H 1981 *Biophys. J.* **35** 193
[15] Chua L 2014 *Semicond. Sci. Technol.* **29** 104001
[16] Rajamani V, Kim H and Chua L 2018 *Sci. China-Inf. Sci.* **61** 060426
[17] Li Q D, Zeng H Z and Li J 2015 *Nonlinear Dyn.* **79** 2295
[18] Guo Z H, Li Z J, Wang M J and Ma M L 2023 *Chin. Phys. B* **32** 038701
[19] Xu Y, Jia Y, Ge M Y, Lu L L, Yang L J and Zhan X 2018 *Neurocomputing* **283** 196
[20] Wu F Q, Wang C N, Jin W J and Ma J 2017 *Physica A* **469** 81
[21] Lv M, Wang C N, Ren G D, Ma J and Song X L 2016 *Nonlinear Dyn.* **85** 1479
[22] Wu J, Xu Y and Ma J 2017 *PLoS One* **12** e0174330
[23] Qi G Y and Wang Z M 2021 *Chin. Phys. B* **30** 120516
[24] Kumar S, Strachan J P and Williams R S 2017 *Nature* **548** 318
[25] Hong Q H, Chen H G, Sun J R and Wang C H 2022 *IEEE Trans. Neural Netw. Learning Syst.* **33** 2106
[26] Bilotta E, Pantano P and Vena S 2017 *IEEE Trans. Neural Netw. Learning Syst.* **28** 1228
[27] Gu S Q, He S B, Wang H H and Du B X 2021 *Chaos, Solitons & Fractals* **143** 110613
[28] Ding D W, Chen X Y, Yang Z L, Hu Y B, Wang M Y, Zhang H W and Zhang X 2022 *Chaos, Solitons & Fractals* **158** 112014
[29] Peng Q Q, Gu S Q, Leng X X and Du B X 2021 *Phys. Scr.* **96** 125217
[30] Xu Q, Huang L P, Wang N, Bao H, Wu H G and Chen M 2023 *Nonlinear Dyn.* **111** 20447
[31] Lin H R, Wang C H, Cui L, Sun Y C, Xu C and Yu F 2022 *IEEE Trans. Ind. Inf.* **18** 8839
[32] Zhang S, Zheng J H, Wang X P, Zeng Z H and He S B 2020 *Nonlinear Dyn* **102** 2821
[33] Xu Q, Liu T, Feng C T, Bao H, Wu H G and Bao B C 2021 *Chin. Phys. B* **30** 128702
[34] Andalibi M, Chandler D 2015 *IEEE Trans. Image Process.* **24** 5060